Time scale for multifragmentation in intermediate energy heavy-ion reactions

D. Fox* and R. T. de Souza
Department of Chemistry and Indiana University Cyclotron Facility, Indiana University, Bloomington, Indiana 47405

T. Glasmacher, L. Phair,† D. R. Bowman,* N. Carlin,‡ C. K. Gelbke, W. G. Gong,† Y. D. Kim,§ M. A. Lisa,† W. G. Lynch, G. F. Peaslee,‖ M. B. Tsang, and F. Zhu¶
National Superconducting Cyclotron Laboratory and Department of Physics and Astronomy, Michigan State University, East Lansing, Michigan 48824
(Received 12 May 1994)

Fragment-fragment correlations are used to probe the spatial-temporal extent of the emitting source in central ^{36}Ar+^{197}Au reactions at E/A=35, 50, 80, and 110 MeV. The experimental two particle correlations are compared both with the Koonin-Pratt two-body formalism as well as a three-body Coulomb trajectory calculation. The spatial-temporal extent of the emitting system decreases with increasing incident energy. Within the context of a three-body Coulomb trajectory model the mean fragment emission time rises sharply as a function of the assumed density of the system until $\rho/\rho_0 \approx 0.3$. If one assumes a fixed density, the extracted mean emission time decreases with increasing assumed charge of the emitting system. Assuming $\rho/\rho_0 \approx 0.3$ the mean emission time τ according to calculations using a three-body Coulomb trajectory model, is $\approx$ 115–135 fm/c at E/A=50 MeV and $\approx$ 75–100 fm/c at E/A=110 MeV. Comparisons with a generalized N-body Coulomb trajectory model demonstrate that the effect of interactions with other emitted particles is negligible. The prediction of a microcanonical model which includes pre-emission correlations between the fragments is compared to the measured correlation function at E/A=110 MeV.

PACS number(s): 25.70.Pq

I. INTRODUCTION

Highly excited nuclear matter can decay by the emission of multiple intermediate mass fragments (IMF's: $3 \leq Z \leq 20$) [1–5]. The experimental observation of multiple fragment emission in intermediate energy heavy-ion collisions has stimulated considerable speculation as to the mechanism underlying this phenomenon. Two radically different scenarios have been proposed. A multifragment final state might result from a nearly simultaneous disintegration of the highly excited system [6–10], or from a series of sequential binary decays [11–15]. In both scenarios, the formation and emission of multiple fragments is substantially enhanced by a reduction in the density of the nuclear system [6–9,15–18]. Such a density reduction might arise due to either a rapid dynamical compression-decompression cycle [6–10] or an increase in the thermal pressure of the system [19–22]. The origin of fragments from a nuclear system at low density might be due to density fluctuations [6,16–18].

Determination of the time scale for fragment emission is useful in distinguishing between dynamical and sequential decay models. Sequential decay models typically require longer mean emission times than dynamical multifragmentation models. While dynamical breakup of an excited nuclear system is predicted to occur on a relatively short time scale, $\tau \leq 100$ fm/c [8–10], the time scale associated with a sequential decay scenario can be considerably longer, $\tau \approx 300$ fm/c for a heavy nucleus with 700 MeV excitation energy [15]. Increasing the excitation energy can lead to a shorter mean emission time, $\tau \approx 80$ fm/c for T=13 MeV [23]. Hence, measurement of the IMF emission time scale is important in characterizing the multifragment decay.

Recently, IMF-IMF correlations have been used to deduce information about the spatial and temporal extent of excited nuclear systems [24–34]. In initial measurements of the IMF emission time scale, mean emission times of 300–700 fm/c were deduced for the reactions ^{18}O+^{nat}Ag, ^{197}Au at E/A=84 MeV [24,35] and ^{22}Ne+Au at E/A=60 MeV [25]. These mean emission times are compatible with sequential emission of the IMF's from a decaying source [15]. These experiments, however, did not provide impact parameter selectivity and might have been biased by incomplete phase space coverage. In contrast, more recent exclusive exper-

*Present address: Chalk River Laboratories, Chalk River, Ontario, Canada K0J 1J0.
†Present address: Lawrence Berkeley Laboratories, University of California, Berkeley, CA 94720.
‡Present address: Instituto de Fisica, Universidade de São Paulo, C. Postal 20516, CEP 01498, São Paulo, Brazil.
§Present address: Physics Department, KEK 1-1 Oho, Tsukua, Ibaraki 305, Japan.
‖Present address: Physics Department, Hope College, Holland, MI 49423.
¶Present address: Brookhaven National Laboratory, Upton, NY 11973.

iments indicated a mean IMF emission time of ≈ 100–125 fm/c, for centrally gated ^{36}Ar+^{197}Au at E/A=35 MeV [26–28] and Kr+Nb at E/A=55–75 MeV [30]. These latter mean IMF emission times are consistent with simultaneous emission of the IMF's [8–10].

To characterize the evolution of the spatial-temporal extent of the decaying system with increasing incident energy, we have measured an excitation function for the system ^{36}Ar+^{197}Au at E/A=50, 80, and 110 MeV. Previously reported values for the mean emission time were based on an assumed value of the source radius [29]. In the present paper we will explore the dependence of IMF-IMF correlation functions on the spatial-temporal extent of the decaying system by comparing the measured correlation functions to model predictions covering a wide range of mean emission times and source size. We will also probe the effect on the correlation functions of additional charged particle emission and pre-emission correlations between the fragments. In this paper, we focus on central collisions where angular momentum effects are significantly reduced [36], and hence distortion of the correlation function due to rotational motion and other collective effects [33,34] should be minimal.

The remainder of this paper is organized as follows. The experimental setup is described in Sec. II. In Sec. III general properties of ^{36}Ar+^{197}Au interactions at E/A=50, 80, and 110 MeV are discussed. The spatial-temporal extent of the emitting source is examined in Sec. IV using both the Koonin-Pratt model and a 3-body Coulomb trajectory model. In Sec. V we consider the effects on the correlation functions from the emission of additional charged particles and from pre-emission correlations between the fragments. The results of the present work are summarized in Sec. VI.

II. EXPERIMENTAL SETUP

The experiment was performed using the K1200 cyclotron at the National Superconducting Cyclotron Laboratory at Michigan State University (MSU). ^{36}Ar beams at E/A=50, 80, and 110 MeV, with an intensity of approximately 1×10^8 particles per second impinged on a ^{197}Au target with an areal density of 1 mg/cm^2. Charged particles emitted into the angular range $9° \leq \theta_{\rm lab} \leq 160°$ were detected using the MSU Miniball array [37]. The trigger condition required that at least two detectors in the Miniball were triggered in order to record an event. Each Miniball element consists of a 4 mg/cm^2 plastic scintillator foil backed by a 2 cm thick CsI(Tl) crystal. Particles which punched through the plastic scintillator foils were identified by atomic number up to Z=18 and by mass number for Z=1 and 2. Particles which stopped in the scintillator foil were recorded, but could not be identified by atomic number. The approximate energy thresholds for particle identification were $E_{\rm th}/A \approx 2$ MeV for Z=3, $E_{\rm th}/A \approx 3$ MeV for Z=10, and $E_{\rm th}/A \approx 4$ MeV for Z=18. Energy calibrations for the forward detectors were obtained by elastic scattering of ^{4}He, ^{6}Li, ^{10}B, ^{12}C, ^{16}O, ^{20}Ne, and ^{35}Cl beams with E/A=4.5 to 20 MeV from a ^{197}Au target. For detectors in rings 1–4, $9° \leq \theta_{\rm lab} \leq 40°$, these calibrations are estimated to be accurate to within 5%.

III. GENERAL PROPERTIES

Intermediate energy heavy-ion collisions can lead to the emission of a large number of charged particles, N_C. At the incident energies studied, the N_C distribution is roughly characterized by a plateau followed by a steeply falling tail. For ^{36}Ar+^{197}Au collisions in the energy range E/A=50–110 MeV the end of the plateau increases from $N_C \approx$20 for E/A = 50 MeV to $N_C \approx$32 for E/A = 110 MeV [29,38]. The IMF multiplicity $N_{\rm IMF}$ increases with both increasing N_C and beam energy [3,39]. For the most central collisions, characterized by high N_C, $\langle N_{\rm IMF} \rangle$ reaches 2, 3, and 4 for E/A=50, 80, and 110 MeV, respectively. The measured charged particle multiplicity may be used as a measure of the centrality of the collision [40]. Small impact parameters b correspond to composite systems with high excitation and consequently large charged particle multiplicity. The approximate degree of centrality of each collision can be determined using a simple geometrical model [41] and the total charged particle multiplicity measured in the Miniball. In this prescription, for each value of N_C the impact parameter b is found in terms of the maximum impact parameter $b_{\rm max}$ for which at least two charged particles are detected in the Miniball. In this paper we will concentrate on central collisions, defined by $b/b_{\rm max} \leq 0.2$, which corresponds to $N_C \geq$21, 27, and 32 for E/A =50, 80, and 110 MeV, respectively.

The energy spectra of boron fragments emitted from ^{36}Ar+^{197}Au collisions at E/A=50, 80, and 110 MeV are presented in Fig. 1. The high energy bump at forward angles in the energy spectra is clear evidence of fragment emission from a projectilelike source. With increasing beam energy the projectilelike component becomes more distinct. At more backward angles the energy spectra fall off roughly exponentially. As seen in Fig. 2, selecting central interactions, $b/b_{\rm max} < 0.20$, essentially eliminates the cross section of boron fragments emitted from the projectilelike source. Elimination of the projectilelike component in the kinetic energy spectra suggests the selection of a more equilibrated single system.

An additional test of the degree to which our multiplicity criterion selects a single source is provided by examination of the angular distribution of IMF's. The angular distributions for selected IMF's from peripheral, $0.70 < b/b_{\rm max} < 0.85$, and central interactions are shown in Fig. 3. For the peripheral interactions, the upper panels, two very clear components of the angular distributions are observed. This two component nature is best observed in the angular distribution of Li fragments at 110 MeV. First, at small angles the angular distributions fall in a steep exponential. This part of the angular distribution is due to emission from a fast projectilelike source. The second component for peripheral interactions is substantially less forward focused. This component may be associated with emission from both an intermediate rapidity source where significant velocity damping has oc-

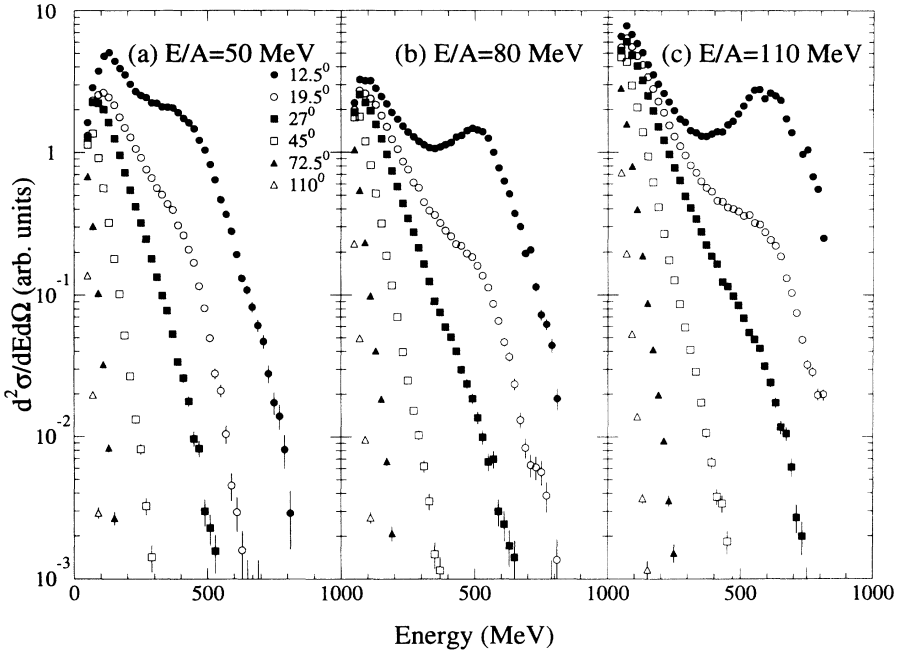

FIG. 1. Inclusive energy spectra for boron fragments emitted from ^{36}Ar+^{197}Au collisions at E/A=50, 80, and 110 MeV at θ_{lab}=12.5°, 19.5°, 27°, 35.5°, 45°, 57.5°, 72.5°, 90°, 110°, and 130°.

curred and a slower moving targetlike source. Selecting on central collisions suppresses the forward peaked component in the angular distribution for all fragments at each of the incident energies. The angular distributions are relatively flat at forward angles, with a sharp drop-off at backward angles particularly for heavy fragments. The sharp drop-off at backward angles may be associated with higher effective thresholds at backward angles due to the momentum of the source in the laboratory frame.

IV. SPATIAL-TEMPORAL EXTENT OF THE EMITTING SYSTEM

In this section we will extract information about the spatial-temporal extent of the emitting system by studying the final-state interaction between two IMF's emitted from the system. The strength of the final-state interaction can be measured by using the two-IMF correlation function $R(v_{red})$ which is defined in terms of the ratio of the coincidence yield, Y_{12}, to the product of the single particle yields, Y_1 and Y_2:

$$\sum_{\mathbf{p}_1,\mathbf{p}_2} Y_{12}(\mathbf{p}_1,\mathbf{p}_2) = C[1+R(v_{red})] \sum_{\mathbf{p}_1,\mathbf{p}_2} Y_1(\mathbf{p}_1)Y_2(\mathbf{p}_2), \quad (1)$$

where $\mathbf{p}_1$ and $\mathbf{p}_2$ are the laboratory momenta of IMF's 1 and 2, v_{red} is the reduced velocity given by $v_{red} = v_{rel}/\sqrt{Z_1+Z_2} = (\mathbf{p}_1/m_1 - \mathbf{p}_2/m_2)/\sqrt{Z_1+Z_2}$, and C is a normalization constant determined by requiring $\langle R(v_{red})\rangle$=0 at large relative momenta where the final state interaction is small. The masses of the IMF's, m_1

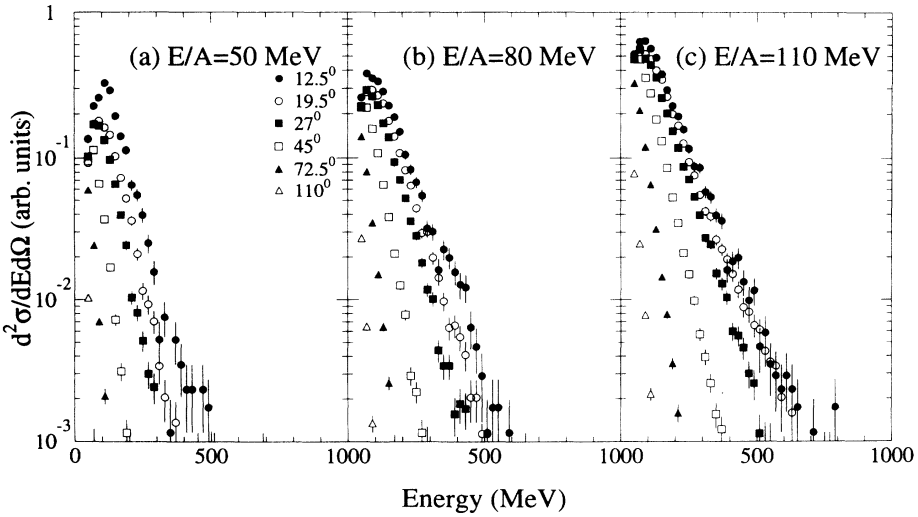

FIG. 2. Energy spectra for boron fragments gated on central ^{36}Ar+^{197}Au collisions, $b/b_{max} < 0.2$, at E/A=50, 80, and 110 MeV at θ_{lab}=12.5°, 19.5°, 27°, 35.5°, 45°, 57.5°, 72.5°, 90°, 110°, and 130°.

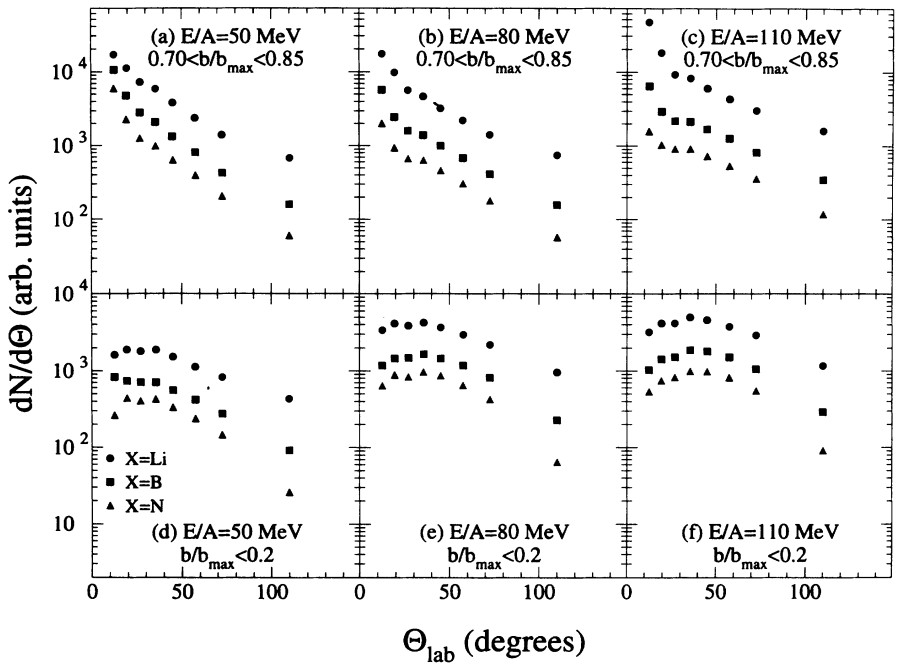

FIG. 3. Angular distributions of Li, B, and N fragments emitted from peripheral (a)–(c), $0.70 < b/b_{max} < 0.85$, and central (d)–(f), $b/b_{max} < 0.2$, $^{36}Ar+^{197}Au$ collisions at E/A=50, 80, and 110 MeV.

and m_2, are assumed to be twice their atomic number times the nucleon rest mass. All correlation functions presented in this paper have been normalized to unity in the region $0.026c \leq v_{red} \leq 0.035c$. Constructing the correlation functions using v_{red} instead of either the relative momentum or the relative velocity allows the data to be summed over all combinations of IMF pairs with $4 \leq Z_1, Z_2 \leq 9$ [27,28].

In previously reported work for $^{36}Ar+^{197}Au$ at E/A=35 MeV [26–28] IMF correlation functions were constructed for IMF pairs in rings 2 and 3 of the Miniball, $16° \leq \theta_{lab} \leq 31°$. In order to increase statistics we have extended the range over which the correlation function is constructed to include ring 4, $31° \leq \theta_{lab} \leq 40°$. To examine the effect, if any, of including ring 4 in the correlation functions we have constructed the IMF correlation functions, for central $^{36}Ar+^{197}Au$ reactions at E/A=110 MeV, for IMF pairs detected in rings 2 and 3, $16° \leq \theta_{lab} \leq 31°$, and IMF pairs detected in rings 2–4, $16° \leq \theta_{lab} \leq 40°$. As shown in Fig. 4, the correlation functions constructed from IMF pairs detected in rings 2 and 3 are very similar to the correlation function constructed from all IMF pairs detected in rings 2–4, $16° \leq \theta_{lab} \leq 40°$. In the remainder of the present work, the correlation functions presented are for IMF's detected in rings 2–4, $16° \leq \theta_{lab} \leq 40°$.

The energy spectra and angular distributions shown in Figs. 1 and 3 clearly indicate the presence of multiple sources of IMF's in peripheral collisions. In constructing the IMF-IMF correlation functions one would like to include only those IMF pairs which come from the same source. In order to examine the source of IMF pairs, we show in Fig. 5 the reduced velocity for IMF pairs detected in the first four rings of the Miniball, $9° \leq \theta_{lab} \leq 40°$, plotted versus the velocity of the center of mass of the IMF pair divided by the beam velocity, v_{12}/v_{beam}. For peripheral collisions, upper panels, three groups of IMF pairs can be distinguished. The three groups are most clearly distinguished at E/A=110 MeV, Fig. 5(c), where the kinematical separation of the projectilelike and targetlike sources is greatest. The first group is centered at $v_{12}/v_{beam} \approx 0.75$ and $v_{red} \approx 0.050c$. For these pairs both IMF's come from the decay of a projectilelike source. The second group, where both IMF's are emitted from a targetlike source, is centered at $v_{12}/v_{beam} \approx 0.25$ and $v_{red} \approx 0.030c$. The final group is centered at $v_{12}/v_{beam} \approx 0.45$ and $v_{red} \approx 0.085c$. This group is composed of "mixed" IMF pairs where one IMF is emitted from a projectilelike source, and the second IMF is emitted from a targetlike source. As the beam energy is reduced, more IMF's from the projectilelike source

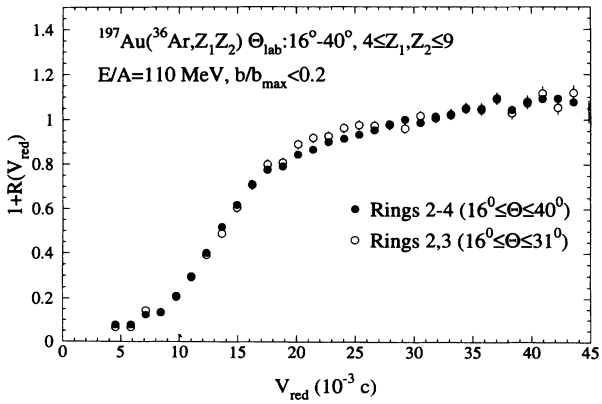

FIG. 4. IMF-IMF correlation functions for Z_1, Z_2 pairs with $4 \leq Z_1, Z_2 \leq 9$, emitted from central $^{36}Ar+^{197}Au$ interactions at E/A=110 MeV for IMF pairs detected in rings 2–4, filled-in points, or in rings 2 and 3, open points.

are detected in the Miniball. This leads to a washing out of the distinction between the three groups of IMF pairs as the relative importance of the first and third groups of IMF pairs increases. For central collisions, Figs. 5(d)–(f), only a single group of IMF pairs is observed. This group is peaked at low $v_{12}/v_{\rm beam}$ and $v_{\rm red}$ corresponding to emission of both IMF's from a targetlike and/or intermediate rapidity source. While there is no evidence of projectilelike fragment pairs, the observed distribution does have a tail which extends into the region corresponding to the emission of mixed pairs. The selection of central collisions significantly reduces the contribution of mixed pairs to the correlation functions. In principle, by gating on the distributions shown in Figs. 5(a)–(c) IMF pairs emitted from the same source in peripheral collisions could be selected. The cleanliness of such gating, however, clearly decreases with decreasing beam energy. In the present paper, we will consider only the relatively clean case of IMF-IMF correlations associated with central collisions.

The strength of the IMF-IMF final state interaction is dependent on the initial spatial-temporal separation of the two fragments. Fragments emitted from a source with a relatively short mean IMF emission time τ will, on average, experience a stronger final state interaction than fragments emitted from a source with a longer mean IMF emission time. Similarly, fragments which are emitted from a source with a small radius R_S will have a stronger final state interaction than fragments emitted from a source with a larger radius. In order to extract information about the mean emission time, comparisons between the experimental correlation functions and theoretical calculations are required.

A. Koonin-Pratt model

In this section we consider the simplest theoretical model, the two particle Koonin-Pratt formalism [42] in which only the final-state interactions between the two emitted IMF's are considered. Effects due to the presence of other charged bodies are assumed to be negligible in the Koonin-Pratt formalism. The validity of this as-

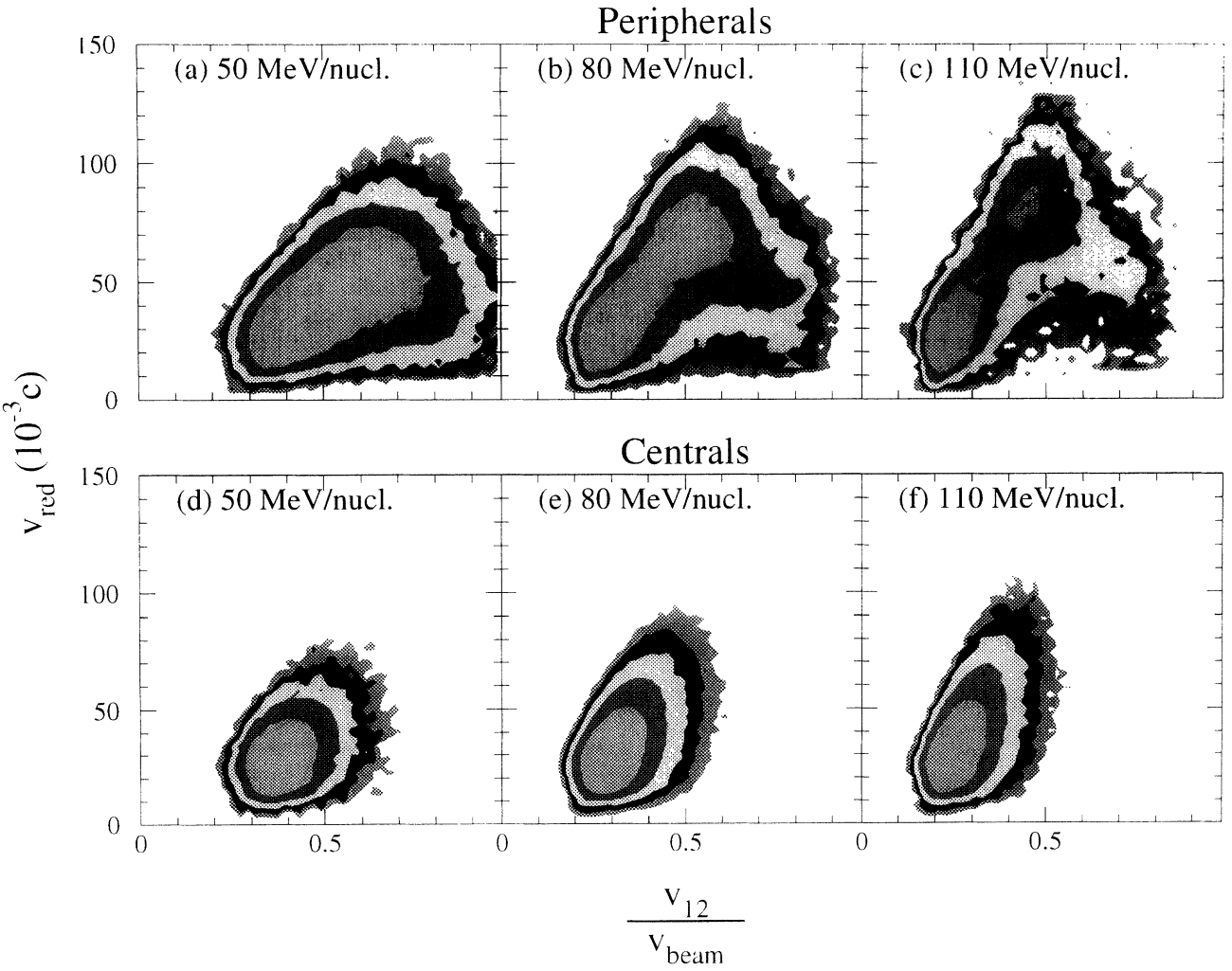

FIG. 5. Reduced velocity $v_{\rm red}$ versus the velocity of the center of mass of the IMF pair divided by the beam velocity, $v_{12}/v_{\rm beam}$, for IMF pairs with $9^\circ \leq \theta_{\rm lab} \leq 40^\circ$ emitted from peripheral (a)–(c) and central ^{36}Ar+^{197}Au collisions (e)–(f).

sumption will be explored in Sec. V.

Previous comparisons between the experimental correlation functions and calculations based on the Koonin-Pratt formalism have been based on a limited number of combinations of the source size R_S defined as the distance between the center of the emitting source and the center of the IMF at emission time, and the mean emission time τ [26–29]. To probe the spatial-temporal extent of the emitting system more fully, we have performed a series of calculations using the Koonin-Pratt formalism. In these calculations, the source size was varied in 0.5 fm steps over the range $5.5 \leq R_S \leq 14$ fm, and the mean emission time was varied in 25 fm/c steps over the range $1 \leq \tau \leq 250$ fm/c. For each calculation, the χ^2 per degree of freedom, χ^2/ν, between the Koonin-Pratt calculation and the experimental correlation function was calculated. In Fig. 6 we show the χ^2/ν for each combination of R_S and τ calculated over the region $0.010c \leq v_{\rm red} \leq 0.030c$, at E/A=35, 50, 80, and 110 MeV. The region below $v_{\rm red} = 0.010c$ has been excluded in calculating the χ^2/ν because the data in this region are affected by the finite angular resolution of the Miniball [26]. Three features are worth noting in Fig. 6. First, at each energy there is a clear valley in χ^2/ν running from very short values of τ and large values of R_S, to larger values of τ and smaller values of R_S. Second, the valley moves towards smaller values of R_S and τ as the beam energy increases indicating a reduction in the spatial-temporal extent of the emitting system with increasing beam energy. Finally at E/A= 80 and 110 MeV the bottom of the valley is sloped, indicating a preference for a smaller physical size of the source, R_S, and a longer mean emission time τ. At lower energies, E/A =35 and 50 MeV, the bottom of the valley is much flatter. To examine more quantitatively the degree to which the Koonin-Pratt formalism describes the experimental final-state interaction, three points along the valley for each beam energy are shown in Fig. 7. While at E/A =80 and 110 MeV the calculations with τ=150 fm/c do a somewhat better job of reproducing the data, all the calculations shown in Fig. 7 do a reasonable job of reproducing the data for $v_{\rm red} \geq 0.010c$.

The values of R_S and τ which yield the best values of χ^2/ν at each beam energy are shown in Table I. The calculations show a clear preference for reducing R_S with increasing beam energy while leaving τ unchanged. A source radius of R_S=5.5 fm at E/A = 110 MeV seems small in comparison to both the radius of a single IMF (2.4–3.1 fm) and the radius of a Au nucleus (≈7 fm). It is hard to imagine a source radius defined by less than the two touching IMF configurations. In addition, it is important to remember that both dynamical multifragmentation models and statistical decay models require a significant reduction in the density of the system in order to produce multiple IMF's [6–9,15–18].

Previous efforts to extract the mean emission time have used a fixed value of R_S [26–29]. To quantify better the dependence of τ on R_S we plot, in Fig. 8, τ as a function of R_S at all four beam energies. The value of

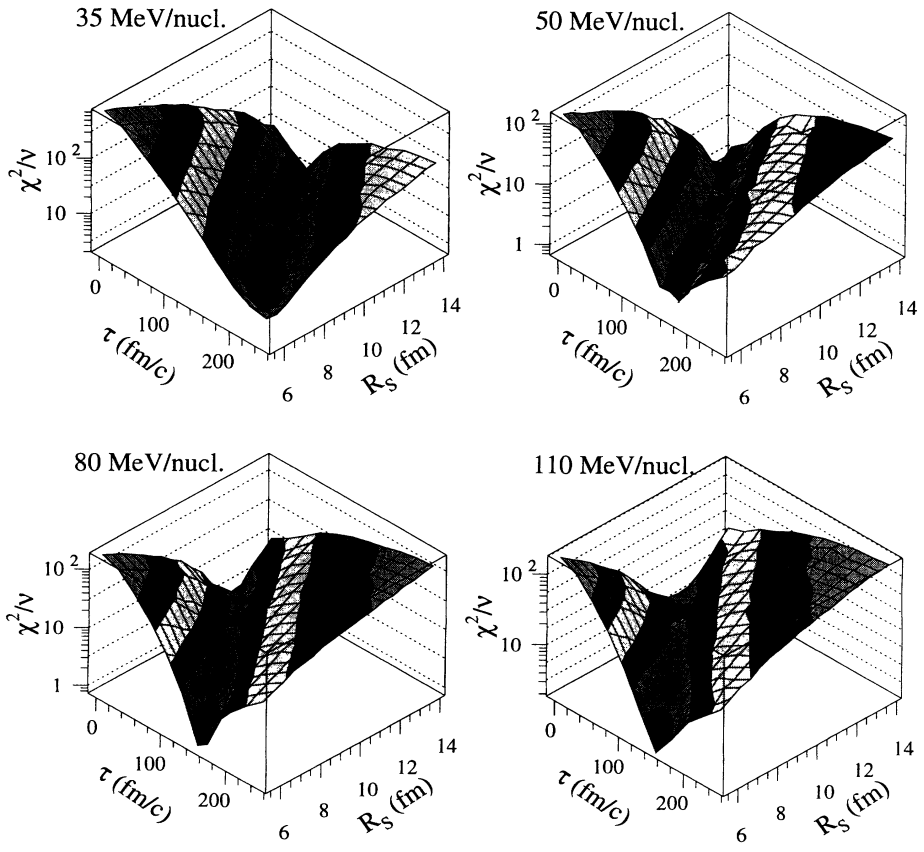

FIG. 6. χ^2 per degree of freedom, χ^2/ν, for the comparisons of Koonin-Pratt calculations to the experimental correlation functions as a function of R_S and τ for central ^{36}Ar+^{197}Au collisions at E/A=35, 50, 80, and 110 MeV.

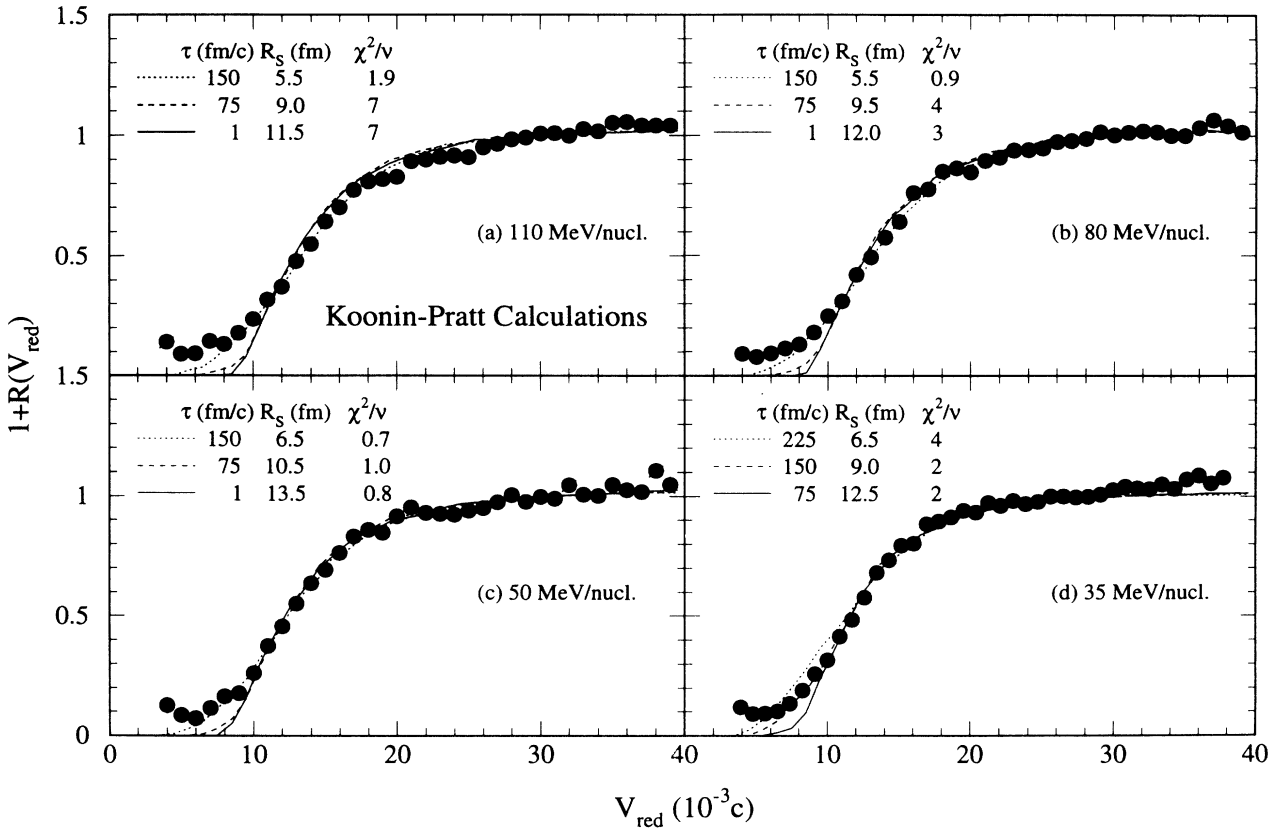

FIG. 7. Comparisons of Koonin-Pratt calculations with the best χ^2/ν values for central ^{36}Ar+^{197}Au collisions at E/A=35, 50, 80, and 110 MeV to the experimental correlation functions.

τ shown in Fig. 8 is the weighted average of the three τ values from the three Koonin-Pratt calculations with the best χ^2/ν for each value of R_S. From Fig. 8 it can be seen that if one assumes a given source radius, as has been done previously [26–29], then τ decreases with increasing beam energy. In order to determine uniquely the mean emission time, an independent measurement of the source radius is required. For any reasonable value of R_S, $R_S \geq R_{\rm IMF1}+R_{\rm IMF2}$, $\tau \leq 225$ fm/c at E/A=35 MeV and ≤ 145 fm/c at E/A=110 MeV. Furthermore, if we assume a reduction in the density of the emitting source, a condition required by theoretical models to account for the observed high fragment yield [6–9,15–18], then for a Au nucleus with $\rho/\rho_0 \approx 0.3$, $R_S \approx 10.5$ fm, we find that $\tau \approx 110$ and 25 fm/c for E/A=35 and 110 MeV, respectively.

TABLE I. Values of R_S and τ which yield the best values of χ^2 per degree of freedom, χ^2/ν, for Koonin-Pratt calculations for central ^{36}Ar+^{197}Au collisions when compared to the measured correlation functions.

E/A (MeV)	τ (fm/c)	R_S (fm)	χ^2/ν
35	150	9.0	2
50	150	6.5	0.7
80	150	6.0	0.7
110	150	5.5	1.9

B. 3-body Coulomb trajectory model

The Koonin-Pratt calculations presented in the previous section involve only the final-state interaction be-

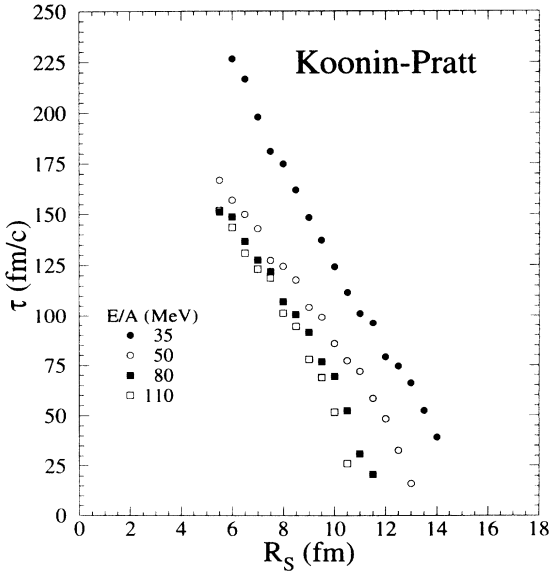

FIG. 8. Mean emission time τ as a function of R_S for central ^{36}Ar+^{197}Au collisions at E/A=35, 50, 80, and 110 MeV.

tween two IMF's emitted from a decaying system. In this section we will use a 3-body Coulomb trajectory model to examine the effect of the emitting system on the IMF-IMF correlation functions. In the 3-body Coulomb trajectory calculation the decaying system, with initial charge Z_S, initial mass number A_S, and radius R_S, emits the first IMF, with initial separation between source and IMF given by $R_S + R_{\rm IMF}$, and then recoils. The trajectories of the emitted IMF and the source residue are calculated up to time t when the second IMF is emitted. The emission time t of the second IMF is assumed to be exponential with a mean time τ. The charge and energy of the two IMF's sample the measured Z distributions and energy spectra. The mass number of each IMF is taken to be twice its atomic number.

Comparison of the experimental energy spectra and the energy spectra calculated by the 3-body Coulomb trajectory model is shown in Fig. 9. The calculated energy spectra are insensitive to the mean emission time. At both $E/A = 50$ and 110 MeV, calculations with a small source, Z_S=40, A_S=96, and R_S=11 do a reasonable job of reproducing the energy spectrum. In contrast, calculations using a larger source, Z_S=79 and A_S=197, fail to reproduce the low energy portion of the spectrum. Assumption of a somewhat larger radius, R_S=12 instead of R_S=9, results in only a slight improvement in the agreement at low energy. These results may suggest a source of considerably reduced charge. The comparison with a source of Z_S=79 is fairly extreme since for central collisions at $E/A = 110$ MeV, $N_C \geq 32$ and $\langle N_{\rm IMF}\rangle \approx 4$. If one assumes half of the charged particles and half of the IMF's are on average emitted before the boron fragment is emitted, a source of $Z \approx 55$ would be expected. Other effects, neglected in the model, such as angular momentum, also enhance the low energy cross section. Since it is our intent to include all of the fragments in the extraction of the emission time scale, we do not wish to impose an energy cut on the data as has been done elsewhere [46]. As a result, the fragment emission time scales extracted represent an average over the entire interaction. Imposition of a common energy threshold above the Coulomb barrier [46] would pose a problem for extraction of the time scale in an excitation function. A single cut on the experimental energy spectrum selects different classes of events with increasing incident energy. Furthermore, while selecting higher energy fragments produces a significant change in the shape of the experimental correlation function [27,46], it produces a negligible change in the results of the trajectory calculation. This insensitivity can be understood since the model does not incorporate phenomena which affect the correlation function such as the decrease in the excitation of the source as particles are emitted.

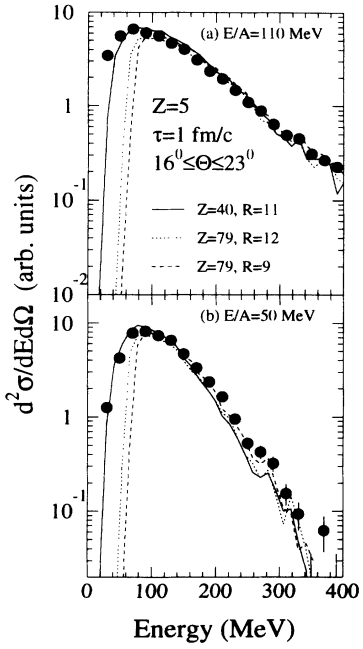

FIG. 9. Comparison of experimental energy spectra of boron fragments associated with central collisions, $b/b_{\rm max} < 0.2$, at $E/A = 50$ MeV/u and 110 MeV/u emitted into the angular range $16° \leq \theta \leq 23°$ with calculations of the 3-body Coulomb trajectory model.

Previously published comparisons between 3-body trajectory calculations and these data were restricted to only a few combinations of R_S and τ [29]. In Fig. 10, χ^2/ν as a function of R_S and τ is shown for comparisons of the 3-body trajectory calculations to the data at E/A=50 and 110 MeV. At each beam energy the calculations have been carried out for two different emitting source sizes, Z_S=40 and A_S=96, and Z_S=79 and A_S=197. As with the Koonin-Pratt calculations, a clear minimum is seen in the χ^2/ν running along the diagonal between the R_S and τ axes; and, for a fixed source size, Z_S and A_S, the spatial-temporal extent of the emitting system decreases with increasing beam energy. The slopes of the χ^2/ν valleys in R_S and τ space are much flatter for the 3-body trajectory calculation than they are for the Koonin-Pratt calculations. This difference may be due to the effect of the heavy residue which is included in the 3-body trajectory calculation, but is ignored in the Koonin-Pratt model. Direct comparisons of the 3-body trajectory calculations with the best values of χ^2/ν to the experimental data are shown in Fig. 11.

The behavior of τ as a function of R_S for the 3-body trajectory calculations is shown in Fig. 12(a). The solid points are for the 3-body trajectory calculations carried out with Z_S=40 and A_S=96, the open points are for Z_S=79 and A_S=197, and the lines show the corresponding results from the Koonin-Pratt formalism. The 3-body trajectory calculations indicate a decrease in the spatial-temporal extent of the emitting system with increasing beam energy. This result is in agreement with the Koonin-Pratt calculations. The 3-body trajectory calculations indicate longer mean emission times than those inferred from the Koonin-Pratt calculations for all cases at E/A=50 MeV and for $R_S > 9.0$ fm at $E/A = 110$ MeV. For smaller source radii the Koonin-Pratt calculations indicate longer mean emission times than the 3-body trajectory calculations for E/A=110 MeV. The 3-body trajectory calculations for the larger initial source, Z_S=79 and A_S=197, show a slightly weaker dependence

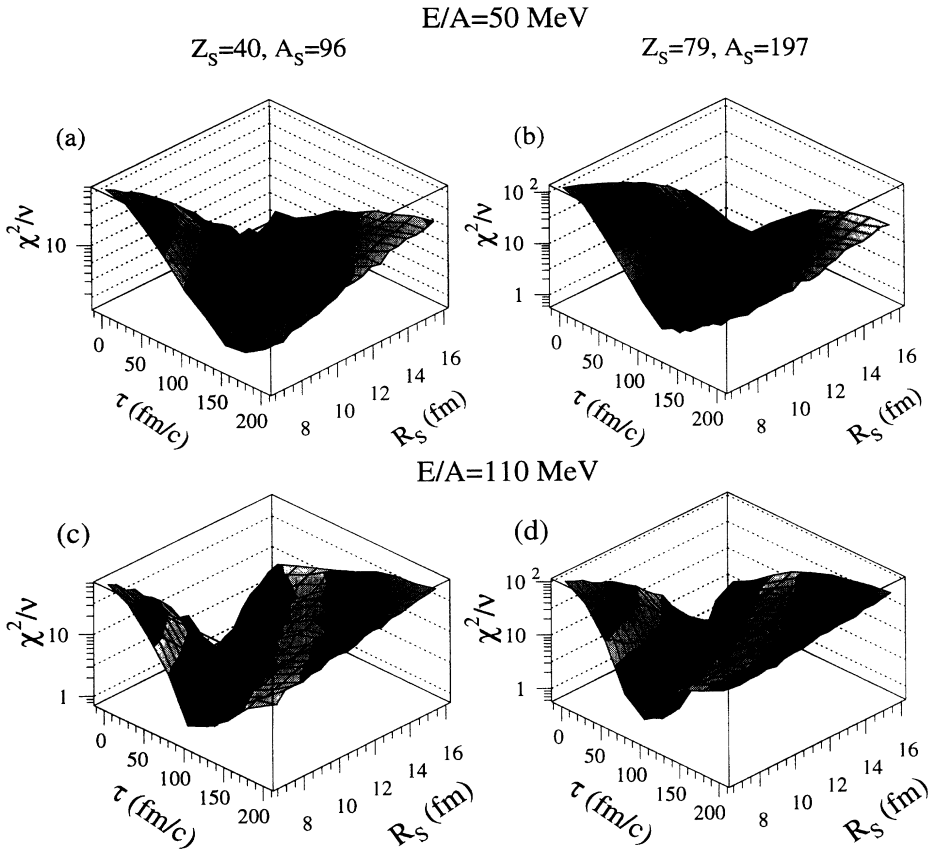

FIG. 10. χ^2/ν for the comparisons of the 3-body trajectory calculations to the experimental correlation functions for central ^{36}Ar+^{197}Au collisions at E/A=50 MeV for (a) Z_S=40, A_S=96 and (b) Z_S=79, A_S=197, and at E/A=110 MeV for (c) Z_S=40, A_S=96 and (d) Z_S=79, A_S=197 as a function of R_S and τ.

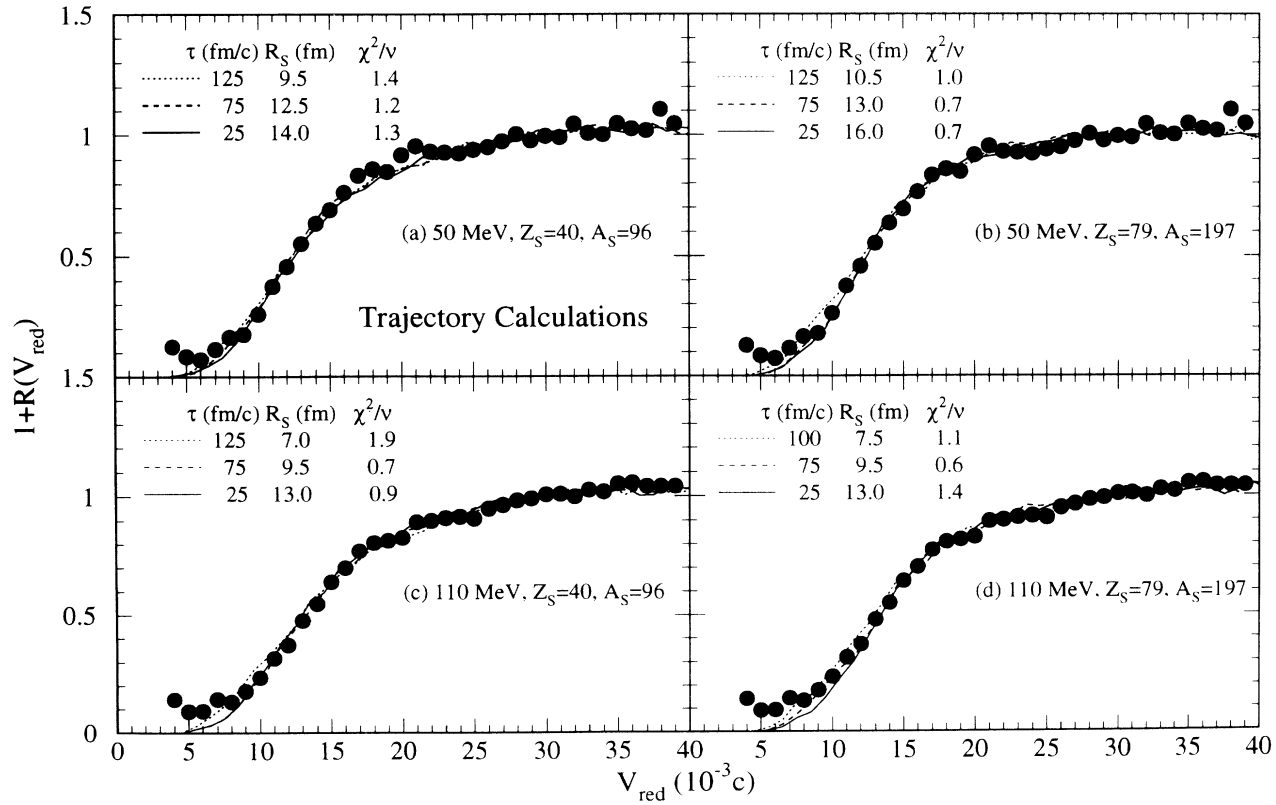

FIG. 11. Comparisons of the 3-body trajectory calculations with the best χ^2/ν values to the experimental correlation functions for central ^{36}Ar+^{197}Au collisions at E/A=50 MeV for (a) Z_S=40, A_S=96 and (b) Z_S=79, A_S=197, and at E/A=110 MeV for (c) Z_S=40, A_S=96 and (d) Z_S=79, A_S=197.

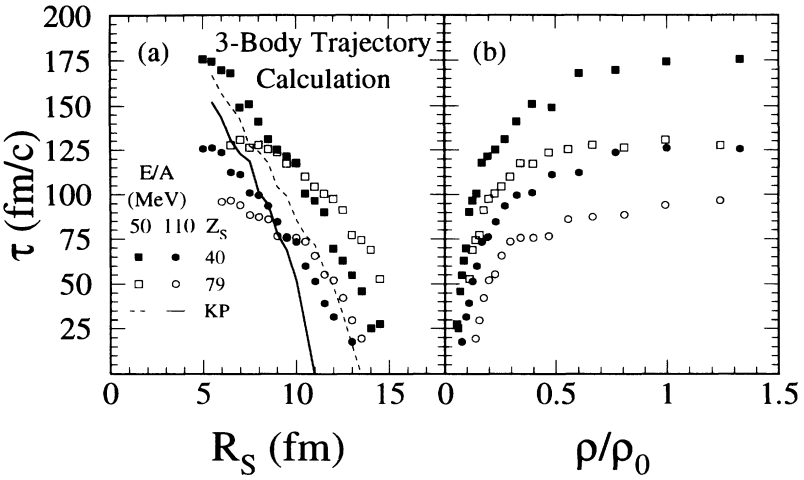

FIG. 12. Mean emission times as a function of (a) R_S and (b) ρ/ρ_0 extracted from the data using a 3-body trajectory model. Extracted mean emission times for central ^{36}Ar+^{197}Au collisions at E/A=50 (squares) and 110 MeV (circles) are shown. The open symbols are for a source with initial Z_S=79 and A_S=197, the solid symbols are for a source with initial Z_S=40 and A_S=96. The lines are for the Koonin-Pratt calculations from Fig. 8.

on R_S than the calculations for the smaller source. Examining the effect of the two different initial choices of Z_S and A_S we see that for $R_S \leq 8$ fm the larger source results in the extraction of a shorter mean emission time, while for R_S >10 fm the larger source indicates a longer mean emission time. In Fig. 12(b) τ has been replotted in terms of the ratio of the density of the decaying system, ρ, to normal nuclear density, ρ_0. For all four cases shown in Fig. 12(b) the mean emission time initially rises steeply with increasing density until $\rho/\rho_0 \approx 0.3$. For $\rho/\rho_0 > 0.3$ the mean emission time is almost independent of the density of the emitting system. Furthermore, for a given density the calculation for the smaller initial source leads to a longer extracted mean emission time. It is interesting to note that many theoretical calculations require freeze out densities of $\approx 0.3\rho_0$. For $\rho/\rho_0 \approx 0.3$, the mean emission time for E/A=50 MeV is 115–135 fm/c. The mean emission time decreases with increasing beam energy to $\tau \approx$75–100 fm/c at E/A=110 MeV.

V. DISCUSSION

The comparisons to both the Koonin-Pratt and 3-body Coulomb trajectory models made in the previous section suggest a decrease in the mean IMF emission time with increasing beam energy. The mean emission times calculated with the Koonin-Pratt model are comparable to the transit time of an Ar projectile past a Au nucleus, $\tau = 45 - 80$ fm/c. A comparison of the mean emission times from the Koonin-Pratt and 3-body Coulomb trajectory models shows that the effect of including a target residue in the calculation is to increase the mean emission time by $\approx$50 fm/c if the residue is assumed to be a Au nucleus and the source has expanded to $\rho/\rho_0 \approx 0.3$. Both model comparisons demonstrate that in the energy range $E/A = 50 - 110$ MeV the mean emission times, $\tau \leq 150$ fm/c, are consistent with emission times expected from dynamical models [8–10] and an expanding-evaporating source model [15,23]. A decrease in the mean IMF emission time with increasing beam energy has also been observed for Kr+Nb reactions at E/A=35–75 MeV [30]. A decreasing mean emission time with increasing beam energy is also consistent with the results of an event shape analysis [43] of central ^{40}Ar+^{51}V reactions at E/A=35–85 MeV [44,45] where it was concluded that a transition between sequential emission and simultaneous multifragmentation occurred.

The above results presented have been obtained using models which consider only two or three fragments. No consideration has yet been given to the presence of other charged bodies and their effect on the correlation functions. While these effects might be expected to be small at low energies where most of the charge is contained in the two observed fragments and a large residue, at higher energies, E/A=110 MeV, an average of four IMF's and at least 28 light charged particles are detected in central collisions [3,39]. Furthermore, the models used in the previous section have ignored the possibility of pre-emission correlations. We will now examine these previously neglected effects.

A. *N*-body trajectory calculations

In order to study possible effects of the interaction of all charged fragments on the correlations functions we have written a generalized N-body Coulomb trajectory code. In these calculations [46], we start with a heavy residue of charge $Z_{\rm res}$ located at the center of a sphere of radius R. The remainder of the initial charge, $Z_{\rm tot}$=97, is then distributed as additional particles based on the measured Z distribution. The particles are assigned random, nonoverlapping positions within the sphere and are emitted simultaneously with an isotropic angular distribution in the center of mass. The masses of all particles are taken from the minimum in the valley of β stability. The initial energy of each fragment is chosen to sample a Maxwell-Boltzmann distribution with temperature T. The trajectories of all charged bodies are then calculated, and the correlation function is constructed based upon the asymptotic momenta of the fragments after filtering for the detector acceptance.

The results of four different N-body calculations with

T=20 MeV, R=11.26 fm are compared in Fig. 13. The four calculations are the following: (a) A full N-body calculation in which the residue, $Z_{res} = 30$, and the equation of motion of all charged bodies are integrated, dashed line. (b) All particles are generated, but the equations of motion are integrated only for the residue, $Z_{res} = 30$, and IMF's with $4 \leq Z \leq 9$, solid line. (c) Only the residue, $Z_{res} = 30$, and two IMF's with $4 \leq Z \leq 9$ are generated and the equations of motion of all three particles are integrated, dash-dotted line. (d) Only the residue, $Z_{res} = 44$, and four IMF's with $4 \leq Z \leq 9$ are generated and the equations of motion of all five particles are integrated, dotted line.

A value of Z_{res}=30 in the N-body Coulomb calculation is comparable to Z_S=40 for the 3-body Coulomb trajectory calculation because Z_S in the 3-body calculation is the charge of the emitting system prior to emission of the IMF's. For all four cases only IMF's with $4 \leq Z \leq 9$ are used to construct the correlation functions.

In Fig. 13 we see very little difference between the four cases described above. The large number of charged particles, included in case (a) and neglected in the other cases has no effect on the correlation function. In addition only tracking two IMF's, case (c), instead of all the IMF's also has a negligible effect on the correlation functions. It can, therefore, be concluded that only the residue and two IMF's need be considered, all other particles have a negligible effect on the correlation functions.

It is important to note that differences between the 3-body and N-body Coulomb trajectory models complicate direct comparison of their results. In the 3-body model the IMF's are emitted from the surface of a sphere with an initial momentum away from the residue. In the N-body calculation all particles are emitted from within the volume of a sphere with no correlation between the position and momentum of the particle. Due to the difference between volume and surface emission a given radius in the N-body calculation corresponds to a smaller radius in the 3-body calculation.

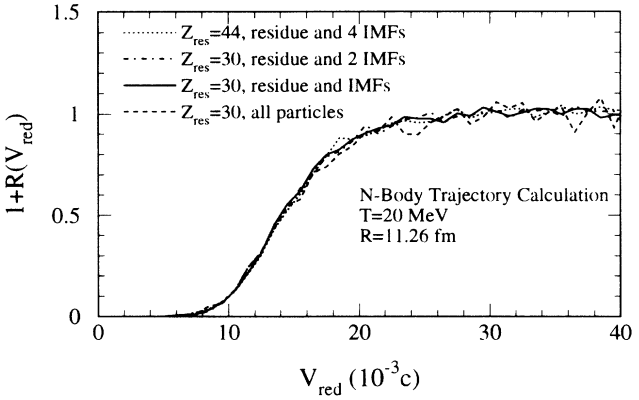

FIG. 13. Results of N-body Coulomb trajectory calculations with T=20 MeV, R=11.26 fm. The dashed line is for the full calculation with Z_{res}=30 in which all charged particles are included, case (a). The other line types represent limited calculations in which only the residue and IMF's with $4 \leq Z \leq 9$ are included in the calculation. For the solid line fragments were formed using the measured Z distribution for all charges, but only those IMF's with $4 \leq Z \leq 9$ were then tracked along with a Z_{res}=30 residue, case (b). The dash-dotted line represents a calculation in which only two IMF's with $4 \leq Z \leq 9$ and the residue, with Z_{res}=30 were considered, case (c). The dotted line is for a calculation with Z_{res}=44 and four IMF's with $4 \leq Z \leq 9$, case (d).

B. Microcanonical model

Recent calculations using the microcanonical model MCFRAG [47,48] have suggested that pre-emission correlations between all fragments in a decaying system play an important role in the correlation functions [49]. In this model, at low excitation energy a bump is produced in the correlation functions at $v_{red} \approx 0.02c$ due to the IMF's starting close together and with their mutial interaction dominating their relative motion. At higher excitation energies the relative motion of the IMF's is dominated by their interactions with the other emitted particles and no bump is seen. Both the Koonin-Pratt and generalized Coulomb trajectory models ignore the possibility of such pre-emission correlations between the fragments. To explore the effect of the pre-emission correlations on the experimentally measured fragment-fragment correlation functions, we will now compare the experimental IMF-IMF correlation functions with predictions from MCFRAG. The model assumes a freeze-out radius of $r_o \approx R_f A^{1/3}$ fm where the initial positions of the fragments are defined and after which they interact only through their mutual Coulomb repulsion. The decay of excited IMF's is not allowed in the calculation. To account roughly for pre-equilibrium emission, the fragmenting system was assumed to be a ^{197}Au nucleus. In Fig. 14(a) the $\langle N_C \rangle$ and $\langle N_{IMF} \rangle$ predicted by MCFRAG are shown as a function of the excitation energy E^* for a freeze out radius of 12.8 fm, R_f=2.2. The multiplicities have been filtered for the Miniball acceptance. To transform each event from the center of mass to the laboratory a center-of-mass velocity, $v_{c.m.}$, of $0.041c$ was used. This value of $v_{c.m.}$ corresponds to 50% linear momentum transfer in the E/A = 110 MeV ^{36}Ar+^{197}Au reaction. The relationship between $\langle N_{IMF} \rangle$ and N_C predicted by MCFRAG is compared to the experimental data in Fig. 14(b). The raw $\langle N_{IMF} \rangle$ vs N_C distribution from MCFRAG is shown as filled-in points, while the effect of filtering the calculation for the detector acceptance is depicted as the open points assuming $v_{c.m.}$ of $0.041c$. The sensitivity of the predicted multiplicities to the kinematical boost are shown as a solid line for $v_{c.m.} = 0.0c$, and a dashed line for $v_{c.m.} = 0.075c$, 100% linear momentum transfer. Also shown in Fig. 14(b) is the measured N_{IMF} vs N_C distribution for E/A = 110 MeV ^{36}Ar+^{197}Au interactions. MCFRAG overpredicts the number of IMF's except at very large N_C. The dramatic effect of the detector thresholds on the predicted fragment multiplicities

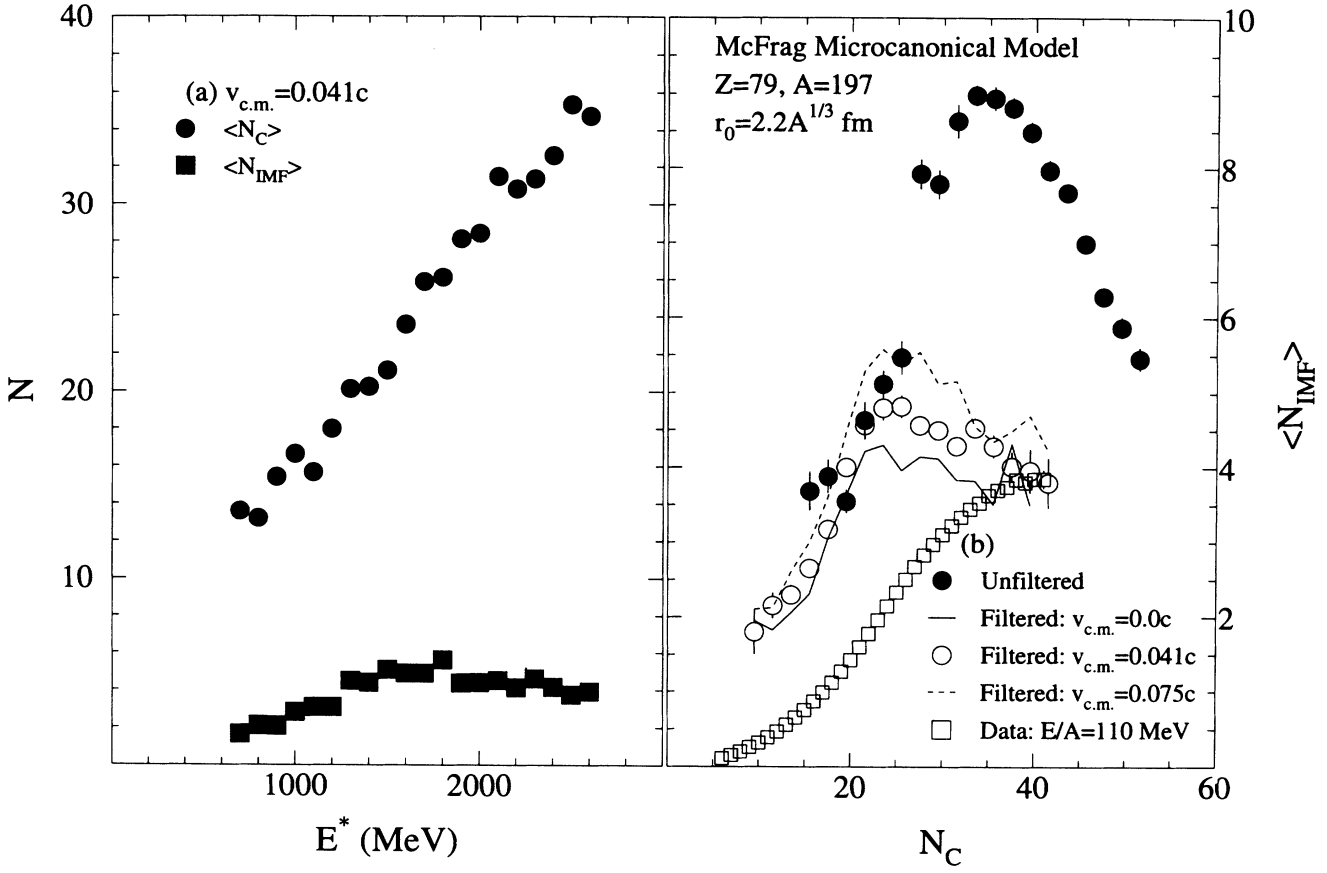

FIG. 14. (a) N_C, circles, and N_{IMF}, squares, as a function of the excitation energy, E^* for the microcanonical model MCFRAG. The calculations have been filtered for the Miniball acceptance assuming $v_{\mathrm{c.m.}} = 0.041c$. (b) Comparison of the N_C vs N_{IMF} distribution from the microcanonical model MCFRAG to the measured data. MCFRAG calculations, unfiltered for the detector acceptance, are shown as solid circles. The McFrag calculations after filtering for the detector acceptance are shown as a solid line for $v_{\mathrm{c.m.}} = 0.0c$, open circles for $v_{\mathrm{c.m.}} = 0.041c$, and a dashed line for $v_{\mathrm{c.m.}} = 0.075c$.

is due to the peaking of the predicted kinetic energy spectra at low energy. More detailed comparisons of kinetic energy spectra with the model predictions are presently underway.

In Fig. 15 the correlation function predicted by MCFRAG is compared to the experimental, 3-body, and N-body correlation functions. For the MCFRAG calculation an excitation energy of $E^* = 2400$ MeV was used so as to reproduce roughly the measured fragment and charged particle multiplicities. The correlation function predicted by MCFRAG is in good agreement with the data. The MCFRAG calculation and the 3-body calculation for a similar source radius and simultaneous fragment emission are in good agreement for all but the very low v_{red} region. At lower excitation energies, $600 \leq E^* \leq 1000$ MeV, MCFRAG predicts a bump in the correlation function, due to pre-emission correlations, at $v_{\mathrm{red}} \approx 0.02c$ [49]. The data shown, however, have no sign of a bump in the correlation function at E/A=35 MeV [26]. Pre-emission correlations do not, therefore, appear to be important for this system at the excitation energy involved in central collisions.

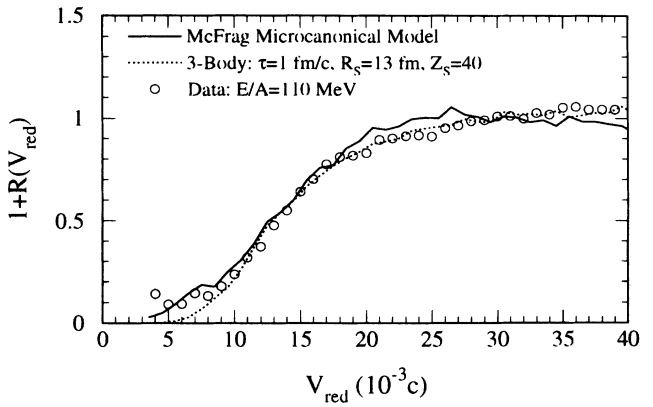

FIG. 15. Comparison of the IMF-IMF correlation function from MCFRAG, solid line, to the 3-body calculation, dotted line, and the measured correlation function at E/A=110 MeV, open circles. The MCFRAG calculation assumes E^*=2400 MeV and a $r_0 = 12.8$ fm. The 3-body calculation is for a source with R_S=13 fm, Z_S=40, and A_S=96 with $\tau = 1$ fm/c.

VI. SUMMARY

The spatial-temporal extent of the emitting source for central $^{36}Ar+^{197}Au$ interactions has been shown to decrease with increasing beam energy. Calculations with a 3-body Coulomb trajectory model show that the extracted mean emission time rises steeply as a function of the assumed density of the emitting system until $\rho/\rho_0 \approx 0.3$. For higher densities the extracted mean emission time is essentially flat as a function of ρ. While extraction of a unique mean emission time requires an independent measure of the source size, or density, we have shown that for any reasonable value of R_S, $R_S \geq R_{\rm IMF1} + R_{\rm IMF2}$, comparing the measured correlation functions to calculations of the Koonin-Pratt model yields $\tau \leq 225$ fm/c at E/A=35 and $\tau \leq 145$ fm/c at E/A=110 MeV. Assuming $\rho/\rho_0 \approx 0.3$ leads to mean emission times of 115–135 and 75–100 fm/c at E/A=50 and 110 MeV, respectively, from comparisons to 3-body Coulomb trajectory calculations and mean emission times of 75 and 25 fm/c at E/A= 50 and 110 MeV, respectively, from comparisons to the Koonin-Pratt model. Calculations with an N-body trajectory code indicates that light charged particles and additional IMF's have a negligible effect on the measured correlation functions. Assuming $E^* = 2400$ MeV and a freeze out radius of 12.8 fm, the microcanonical model MCFRAG is able to reproduce the measured correlation function for E/A=110 MeV. At lower incident energies, however, the data show no evidence of a bump in the correlation function at $v_{\rm red} \approx 0.02c$ due to the pre-emission correlations predicted by MCFRAG.

ACKNOWLEDGMENTS

We would like to thank Prof. D. H. E. Gross for making his microcanonical code MCFRAG available to us and for his helpful comments. We would like to acknowledge the valuable assistance of the staff and operating personnel of the K1200 cyclotron at the National Superconducting Cyclotron Laboratory for providing the high quality beams which made this experiment possible. This work was supported by the U.S. Department of Energy under DE-FG02-92ER40714 and the National Science Foundation under Grants No. PHY-89-13815 and No. PHY-90-15957.

[1] J. W. Harris, B. V. Jacak, K.-H. Kampert, G. Claesson, K. G. R. Doss, R. Ferguson, A. I. Gavron, H.-A. Gustafsson, H. Gutbrod, B. Kolb, F. Lefebrres, A. M. Poskanzer, H.-G. Ritter, H. R. Schmidt, L. Teitelbaum, M. Tincknell, S. Weiss, H. Wieman, and J. Wilhelmy, Nucl. Phys. **A471**, 241c (1987).

[2] K. G. R. Doss, H.-A. Gustafsson, H. Gutbrod, J. W. Harris, B. V. Jacak, K.-H. Kampert, B. Kolb, A. M. Poskanzer, H.-G. Ritter, H. R. Schmidt, L. Teitelbaum, M. Tincknell, S. Weiss, and H. Wieman, Phys. Rev. Lett. **59**, 2720 (1987).

[3] R. T. de Souza, L. Phair, D. R. Bowman, N. Carlin, C. K. Gelbke, W. G. Gong, Y. D. Kim, M. A. Lisa, W. G. Lynch, G. F. Peaslee, M. B. Tsang, H. M. Xu, and F. Zhu, Phys. Lett. B **268**, 6 (1991).

[4] C. A. Ogilvie, J. C. Adloff, M. Begemann-Blaich, P. Bouissou, J. Hubele, G. Imme, I. Iori, P. Kreutz, G. J. Kunde, S. Leray, V. Lindenstruth, Z. Liu, U. Lynen, R. J. Meijer, U. Milkau, W. F. J. Müller, C. Ngô, J. Pochodzalla, G. Raciti, G. Rudolf, H. Sann, A. Schüttauf, W. Seidel, L. Stuttge, W. Trautmann, and A. Tucholski, Phys. Rev. Lett. **67**, 1214 (1991).

[5] D. R. Bowman, G. F. Peaslee, R. T. de Souza, N. Carlin, C. K. Gelbke, W. G. Gong, Y. D. Kim, M. A. Lisa, W. G. Lynch, L. Phair, M. B. Tsang, C. Williams, N. Colonna, K. Hanold, M. A. McMahan G. J. Wozniak, L. G. Moretto, and W. A. Friedman, Phys. Rev. Lett. **67**, 1527 (1991).

[6] W. Bauer, G. F. Bertsch, and S. Das Gupta, Phys. Rev. Lett. **58**, 863 (1987).

[7] K. Sneppen and L. Vinet, Nucl. Phys. **A480**, 342 (1988).

[8] J. Aichelin, G. Peilert, A. Bohnet, A. Rosenhauer, H. Stöcker, and W. Greiner, Phys. Rev. C **37**, 2451 (1988).

[9] G. Peilert, H. Stöcker, W. Greiner, A. Rosenhauer, A. Bohnet, and J. Aichelin, Phys. Rev. C **39**, 1402 (1989).

[10] D. H. Boal and J. N. Glosli, Phys. Rev. C **37**, 91 (1988).

[11] L. G. Moretto, Nucl. Phys. **A247**, 211 (1975).

[12] W. A. Friedman and W. G. Lynch, Phys. Rev. C **28**, 16 (1983).

[13] W. A. Friedman and W. G. Lynch, Phys. Rev. C **28**, 950 (1983).

[14] W. A. Friedman, Phys. Rev. C **40**, 2055 (1989).

[15] W. A. Friedman, Phys. Rev. C **42**, 667 (1990).

[16] A. Vicentini, G. Jaucci, and V. R. Pandharipande, Phys. Rev. C **31**, 1783 (1985).

[17] R. J. Lenk and V. R. Pandharipande, Phys. Rev. C **34**, 177 (1986).

[18] T. J. Schlagel and V. R. Pandharipande, Phys. Rev. C **36**, 162 (1987).

[19] G. Bertsch and P. J. Siemens, Phys. Lett. **126B**, 9 (1983).

[20] H. Sagawa and G. F. Bertsch, Phys. Lett. **155B**, 11 (1985).

[21] H. Schulz, B. Kämpfer, H. W. Barz, G. Röpke, and J. Bondorf, Phys. Lett. **147**B, 17 (1984).

[22] S. Levit and P. Bonche, Nucl. Phys. **A437**, 426 (1984).

[23] W. A. Friedman, in *Proceedings of the International Symposium Towards a Unified Picture of Nuclear Dynamics, Nikko, Japan, 1991*, edited by Y. Abe, S. M. Lee, and F. Sakata, AIP Conf. Proc. No. 250 (AIP, New York, 1992), p. 422.

[24] R. Trockel, U. Lynen, J. Pochodzalla, W. Trautmann, N. Brummund, E. Eckert, R. Glasow, K. D. Hildenbrand, K. H. Kampert, W. F. J. Müller, D. Pelte, H. J. Rabe, H. Sann, R. Santo, H. Stelzer, and R. Wada, Phys. Rev. Lett. **59**, 2844 (1987).

[25] R. Bougault, J. Colin, F. Delaunay, A. Genoux-Lubain, A. Hajfani, C. Le Brun, J. F. Lecolley, M. Louvel, and J. C. Steckmeyer, Phys. Lett. B **232**, 291 (1989).

[26] Y. D. Kim, R. T. de Souza, D. R. Bowman, N. Carlin, C. K. Gelbke, W. G. Gong, W. G. Lynch, L. Phair, M.

B. Tsang, F. Zhu, and S. Pratt, Phys. Rev. Lett. **67**, 14 (1991).

[27] Y. D. Kim, R. T. de Souza, C. K. Gelbke, W. G. Gong, and S. Pratt, Phys. Rev. C **45**, 387 (1992).

[28] Y. D. Kim, R. T. de Souza, D. R. Bowman, N. Carlin, C. K. Gelbke, W. G. Gong, W. G. Lynch, L. Phair, M. B. Tsang, and F. Zhu, Phys. Rev. C **45**, 338 (1992).

[29] D. Fox, R. T. de Souza, L. Phair, D. R. Bowman, N. Carlin, C. K. Gelbke, W. G. Gong, Y. D. Kim, M. A. Lisa, W. G. Lynch, G. F. Peaslee, M. B. Tsang, and F. Zhu, Phys. Rev. C **47**, R421 (1993).

[30] E. Bauge, A. Elmaani, Roy A. Lacey, J. Lauret, N. N. Ajitanand, D. Craig, M. Cronqvist, E. Gualtieri, S. Hannuschke, T. Li, B. Llope, T. Reposeur, A. Vander Molen, G. D. Westfall, J. S. Winfield, J. Yee, S. Yennello, A. Nadasen, R. S. Tickle, and E. Norbeck, Phys. Rev. Lett. **70**, 3705 (1993).

[31] T. C. Sangster, M. Begemann-Blaich, Th. Blaich, H. C. Britt, A. Elmaani, N. N. Ajitanand, and M. N. Namboodiri, Phys. Rev. C **47**, R2457 (1993).

[32] D. R. Bowman, G. F. Peaslee, N. Carlin, R. T. de Souza, C. K. Gelbke, W. G. Gong, Y. D. Kim, M. A. Lisa, W. G. Lynch, L. Phair, M. B. Tsang, C. Williams, N. Colonna, K. Hanold, M. A. McMahan, G. J. Wozniak, and L. G. Moretto, Phys. Rev. Lett. **70**, 3534 (1993).

[33] T. Ethvignot, J. M. Alexander, A. J. Cole, A. Elmaani, P. Désesquelles, H. Elhage, A. Giorni, D. Heuer, S. Kox, A. Lleres, F. Merchez, C. Morand, D. Rebreyend, P. Stassi, J. B. Viano, F. Benrachi, B. Chambon, B. Cheynis, D. Drain, and C. Pastor, Phys. Rev. C **48**, 618 (1993).

[34] B. Kämpfer *et al.* (FOPI Collaboration), Phys. Rev. C **48**, R955 (1993).

[35] The mean emission time τ and the "half-life" for intermediate mass fragment (IMF) emission, $\tau_{\text{IMF-IMF}}$, defined in Ref. [24], are related as $\tau = 1.44\tau_{\text{IMF-IMF}}$.

[36] L. Phair, D. R. Bowman, N. Carlin, C. K. Gelbke, W. G. Gong, Y. D. Kim, M. A. Lisa, W. G. Lynch, G. F. Peaslee, R. T. de Souza, M. B. Tsang, C. Williams, and F. Zhu, Nucl. Phys. **A564**, 453 (1993).

[37] R. T. de Souza, N. Carlin, Y. D. Kim, J. Ottarson, L. Phair, D. R. Bowman, C. K. Gelbke, W. G. Gong, W. G. Lynch, R. A. Pelak, T. Peterson, G. Poggi, M. B. Tsang, and H. M. Xu, Nucl. Instrum. Methods Phys. Res. Sect. A **295**, 109 (1990).

[38] R. T. de Souza, D. Fox, W. A. Friedman, L. Phair, D. R. Bowman, C. K. Gelbke, W. G. Gong, Y. D. Kim, M. A. Lisa, W. G. Lynch, G. F. Peaslee, M. B. Tsang, and F. Zhu, Phys. Lett. B **300**, 29 (1993).

[39] L. Phair, W. Bauer, D. R. Bowman, N. Carlin, R. T. de Souza, C. K. Gelbke, W. G. Gong, Y. D. Kim, M. A. Lisa, W. G. Lynch, G. F. Peaslee, M. B. Tsang, C. Williams, F. Zhu, N. Colonna, K. Hanold, M. A. McMahan, G. J. Wozniak, and L. G. Moretto, Phys. Lett. B **285**, 10 (1992).

[40] L. Phair, D. R. Bowman, C. K. Gelbke, W. G. Gong, Y. D. Kim, M. A. Lisa, W. G. Lynch, G. F. Peaslee, R. T. de Souza, M. B. Tsang, and F. Zhu, Nucl. Phys. **A548**, 489 (1992).

[41] C. Cavata, M. Demoulins, J. Gosset, M. C. Lemaire, D. L'Hôte, J. Poitou, and O. Valette, Phys. Rev. C **42**, 1760 (1990).

[42] W. G. Gong, W. Bauer, C. K. Gelbke, and S. Pratt, Phys. Rev. C **43**, 781 (1991).

[43] J. A. López and J. Randrup, Nucl. Phys. **A491**, 477 (1989).

[44] D. A. Cebra, S. Howden, J. Karn, A. Nadasen, C. A. Ogilvie, A. Vander Molen, G. D. Westfall, W. K. Wilson, J. S. Winfield, and E. Norbeck, Phys. Rev. Lett. **64**, 2246 (1990).

[45] H. W. Barz, D. A. Cebra, H. Schulz, and G. D. Westfall, Phys. Lett. B **267**, 317 (1991).

[46] T. Glasmacher, C. K. Gelbke, and S. Pratt, Phys. Lett. B **314**, 265 (1993).

[47] X. Z. Zhang, D. H. E. Gross, S. Y. Xu, and Y. M. Zheng, Nucl. Phys. **A461**, 641 (part I) (1987); **A461**, 668 (part II) (1987).

[48] D. H. E. Gross, Rep. Prog. Phys. **53**, 605 (1990), and references therein.

[49] O. Schapiro, A. R. DeAngelis, and D. H. E. Gross, Report HMI 1993/P1-Schap 1, 1993.

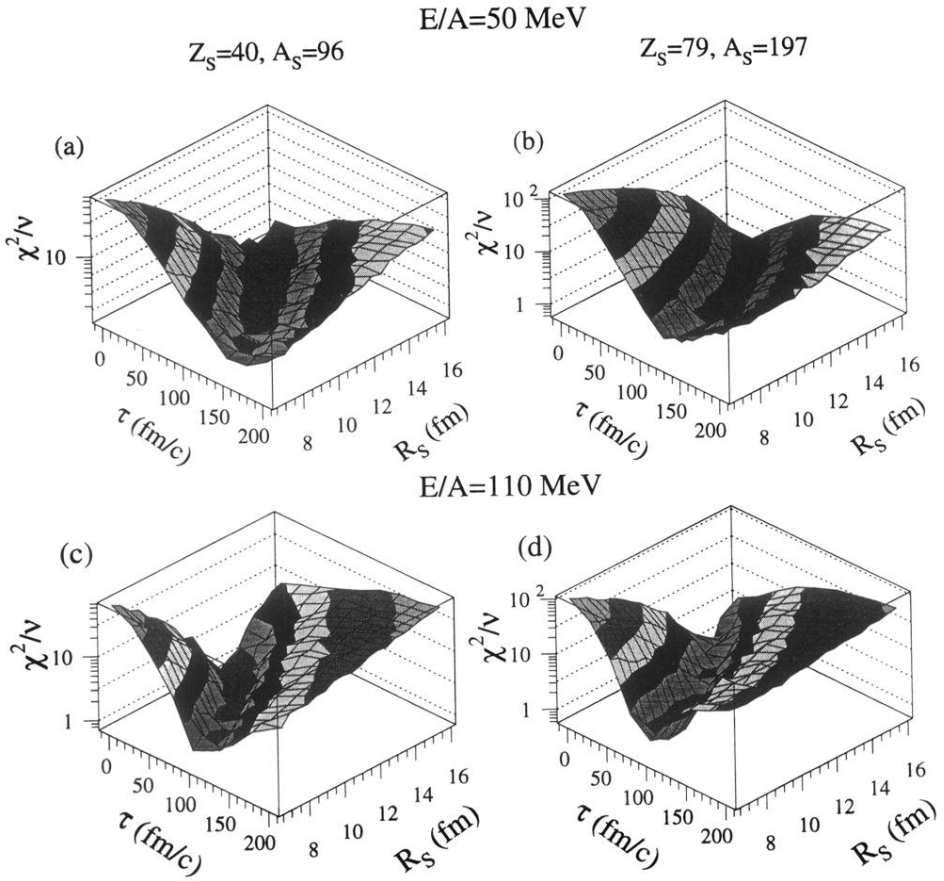

FIG. 10. χ^2/ν for the comparisons of the 3-body trajectory calculations to the experimental correlation functions for central ^{36}Ar+^{197}Au collisions at E/A=50 MeV for (a) Z_S=40, A_S=96 and (b) Z_S=79, A_S=197, and at E/A=110 MeV for (c) Z_S=40, A_S=96 and (d) Z_S=79, A_S=197 as a function of R_S and τ.